physica status solidi (a)

RESEARCH ARTICLE OPEN ACCESS

Modeling and Impedance Spectroscopy Analysis of a High-Efficiency Graphene-Based Heterostructure Solar Cell Exceeding 22% Power Conversion Efficiency

George G. Njema[1] | Abderrahmane Elmelouky[2] | Chinedu C. Ahia[3] | Edson L. Meyer[3] | Joshua K. Kibet[1]

[1]Department of Chemistry, Egerton University, Egerton, Kenya | [2]Laboratory Physics of Condensed Matter (LPMC), University of Chouaib Doukkali, El-Jadida, Morocco | [3]University of Fort Hare, Institute of Technology, Alice, South Africa

Correspondence: Chinedu C. Ahia (chinedu@aims.ac.za)

Received: 6 August 2025 | **Revised:** 5 December 2025 | **Accepted:** 22 December 2025

Keywords: Cole–Cole relaxation | complex conductivity | dielectric relaxations | green energy | photovoltaic

ABSTRACT

The transition to green energy is essential in mitigating climate change and reducing environmental impacts. Although solar energy is a limitless and sustainable resource, photovoltaic technology has yet to achieve its fullpotential due to stability and durability challenges. Herein, a novel solar cell architecture—FTO/AZO/*p*-C_2N/Spiro-OMeTAD/Ni—is investigated using the solar cell capacitance device simulator (SCAPS-1D) and impedance spectroscopy. The performance metrics obtained from the model cell were: open circuit voltage (V_{oc}) of 1.3030 V, short-circuit current (J_{sc}) of 23.23 mA/cm^2, fill factor of 73.84%, and power conversion efficiency of 22.35%. At a bandgap of 1.4 eV of the absorber, quantum efficiency (QE) reached maximum (100%) in the entire wavelength range (300 – 700 nm) but decreased with increasing bandgap of the absorber. At a wavelength of 360 nm, the QE reached 100% with a donor density of between 10^{15} and 10^{20} cm^{-3}. In order to gain deeper insight into the mechanisms of charge storage and light-to-electricity conversion, this study also focused on the analysis of complex impedance (Z^*) and complex conductivity (σ^*). A theoretical investigation of the imaginary components (Z'' and σ'') across a wide frequency range revealed the presence of multiple relaxation processes. Through spectral extrapolation and deconvolution, three distinct relaxation phenomena were identified in both Z^* and σ^*, resembling the Cole–Cole-type relaxations typically associated with Maxwell–Wagner–Sillars effects. These findings suggest localized electrical interactions between active sites along the graphene molecular chains and counterions at interfacial boundaries, leading to induced dipole moments and potential diffusion-driven dynamics. The modeling and understanding of dielectric relaxations and conduction mechanisms provide valuable insights into the underlying phenomena and support the optimization of cell performance.

1 | Introduction

In a rapidly evolving energy landscape, the transition to green energy has gained remarkable momentum, driven by the urgent need to combat global climate change, reduce environmental degradation, and spur climate action. Among renewable sources, solar energy stands out as the most sustainable and promising solution for powering the world indefinitely. However, photovoltaic (PV) technology still faces significant bottlenecks in reaching its full potential [1, 2]. This work introduces a groundbreaking solar cell architecture with a novel *p*-C_2N photoactive layer, designed to enhance performance, stability, and device longevity. Studies on solar cell structures based on C_2N are still few in the PV technology. Herein, an innovative solar cell design demonstrating significant improvements in performance and highlighting the potential of *p*-C_2N-based solar cells in the future PV landscape is presented. The material exhibits excellent optical

and electronic properties, making it an ideal candidate for absorber layers in solar cells. Its high light absorption capabilities ensure that more sunlight is converted into electricity.

This study introduces a novel solar cell architecture that leverages *p*-type carbon nitride as the photoactive layer. Importantly, the use of graphene aligns with the global movement toward sustainable energy solutions. As a carbon-based material, graphene offers an environmentally friendly alternative to conventional materials, supporting the development of greener technologies [3]. Technological relevance of graphene-based solar cells lies in their rapid efficiency advancements, cost-effective processing, and versatile material options. The integration of advanced materials like graphene not only enhances the performance of these solar cells but also aligns with the ongoing quest for sustainable energy solutions, positioning perovskite solar cells (PSC) as a promising option for the future of solar energy. In-depth analysis of the present cell architecture has been performed using electrochemical impedance spectroscopy (EIS) in order to understand the charge carrier mechanisms at interfaces. This is particularly important in semiconductor devices, where interfaces such as absorber/electron transport layer (ETL) and absorber/hole transport layer (HTL) significantly influence device performance. Impedance spectroscopy (IS) enables the detection of interfacial charge accumulation, charge extraction efficiency, and potential defects that could lead to performance degradation [4]. Further, by measuring frequency-dependent impedance responses, IS can reveal the presence of defects and trap states, which hinder carrier transport and contribute to recombination losses [5].

In the present model cell structure, fluorine-doped tin oxide (FTO) is utilized as the transparent conductive oxide (TCO) layer in most PV devices, acting as the front electrode [6]. Its transparency allows light to pass through and reach the active layers, while its conductive properties enable the efficient transport of electricity. FTO boasts a wide bandgap ranging from 3.2 to 4.0 eV, which is essential for maintaining its transparency to visible light [7]. The carrier mobility of FTO, typically between 10 and 50 cm^2/Vs, is sufficient for its role in collecting and transporting charge carriers generated in the active layer [8]. FTO is chosen for its transparency, which is essential for allowing light to penetrate to the active layers. Its conductivity provides an effective pathway for electrons to travel to the external circuit [9]. Moreover, FTO is chemically stable and robust under operating conditions, ensuring long-term durability.

With a bandgap of approximately 2.8 eV, Spiro-OMeTAD HTL has excellent energy alignment with the valence band of the photoactive layer, remains transparent, allowing light to reach the active layer without significant absorption [10]. Despite having a relatively low hole mobility of around 10^{-4}–10^{-3} cm^2/Vs, this is adequate for its role in thin-film devices where distances are relatively short [11]. Its compatibility with solution-based processing techniques makes it suitable for integration into graphene-based and hybrid materials, allowing for smooth film formation that ensures excellent interfacial contact with adjacent layers [12]. Accordingly, organic materials like Spiro-OMeTAD also present advantages in scalability, particularly for lightweight or flexible devices, where processing ease is critical [9]. Conversely, Aluminum-doped Zinc Oxide (AZO) is a transparent conducting oxide critical for optoelectronics, boasting a wide bandgap (3.7 eV), strong electrical conductivity, and significant absorption coefficients in the visible spectrum ($\sim 10^4$ cm^{-1}) [13]. Nickel (Ni) serves as the back electrode, collecting electrons and facilitating their transport to the external circuit [14]. As a metal, nickel lacks a bandgap but has a work function around 5.15 eV, making it suitable for good electrical contact with the hole transport layer [15]. Nickel has a high carrier mobility of between 10^2 and 10^3 cm^2/Vs, which ensures efficient electron transport [16]. Its suitable work function helps form a robust ohmic contact with adjacent layers, enhancing overall device performance.

p-C_2N is an emerging nitrogen-rich two-dimensional semiconductor that has attracted considerable attention for its strong photoactive behavior. Its structure consists of a porous, atomically thin network of carbon and nitrogen atoms arranged in a conjugated lattice, a configuration that gives the material a large surface area, enhanced electronic delocalization, and naturally *p*-type conductivity. The incorporation of nitrogen atoms significantly influences the electronic structure by introducing electron-rich sites and creating favorable hybridization between the valence and conduction band states. *p*-C_2N typically exhibits a direct or quasi-direct bandgap within the visible-light range (∼1.6–2.0 eV) depending on synthesis route and computational model [17]. Optically, the material displays strong absorption in the UV–visible region due to its extended π-conjugation and 2D confinement, which enhances light–matter interactions [18]. This combination of broad spectral absorption and tunable bandgap makes *p*-C_2N suitable for applications where efficient light harvesting is required, such as photodetectors, photocatalytic systems, and next-generation solar cell designs [18]. Another key advantage of *p*-C_2N is its chemical and thermal robustness. The strong covalent C—N bonding provides structural stability under illumination, thermal cycling, and exposure to reactive environments [17]. This makes the material more durable than many organic semiconductors and well-suited for long-term operation in energy conversion and sensing systems.

Two-dimensional porous carbon nitride (C_2N), also known as h2D-C_2N, has gained attention as a versatile semiconducting material owing to its distinctive holey structure composed of alternating benzene and pyrazine rings, which form a planar, covalent framework with tunable electronic properties [19, 20]. Computational studies using hybrid density functional theory methods report a direct bandgap of approximately 2.47 eV for monolayer C_2N, while experimental measurements on multilayer films indicate an optical bandgap near 1.96 eV, which decreases with increasing layer thickness [19–21]. The electronic structure features flat bands near the valence and conduction edges, largely derived from nitrogen orbitals, influencing carrier effective masses and transport characteristics [22]. C_2N exhibits strong absorption in the visible spectrum, with significant excitonic effects in few-layer forms, where exciton binding energies can exceed 0.6 eV, making it suitable for optoelectronic and photocatalytic applications [20]. Field-effect transistor studies on multilayer C_2N demonstrate high on/off current ratios ($\sim 10^7$), though intrinsic carrier mobilities for monolayers remain largely unexplored [21]. Recent theoretical work also predicts the possibility of higher-order topological insulating phases, expanding their potential in novel electronic architectures [22]. Collectively, its tunable bandgap, robust optical absorption, and structural stability highlight C_2N as a promising material for integration in 2D heterostructures, hybrid absorbers, and PV or photocatalytic systems.

In solar cell applications, the graphene family of materials significantly enhances the efficiency and stability of various solar cells, including organic (OPVs), dye-sensitized solar cells, and PSCs [23]. *P*-type conductivity in C_2N remains largely elusive and experimentally unconfirmed due to several factors. First, Fermi level pinning at interfaces with common electrodes tends to align the Fermi level toward the conduction band, favoring electron conduction and making hole injection challenging [24]. Second, there is a lack of experimental studies on controlled doping; no reports, to date, demonstrate stable hole-doped C_2N through acceptor impurities or chemical doping combined with transport measurements [25]. Further, much of the existing research on C_2N focuses on applications such as sensors, composites, or optoelectronic devices, rather than on investigating intrinsic *p*-type transport properties. Theoretical studies suggest doping strategies, but practical realization may be hindered by structural instability, trap states, Fermi-level pinning, and recombination effects, all of which could impede the achievement of reliable *p*-type conduction. Pristine C_2N has been synthesized and characterized as a semiconducting 2D material with a bandgap of approximately 1.7–1.96 eV, and devices such as field-effect transistors (FETs) have been fabricated, showing high on/off ratios. However, these studies do not report stable hole conduction or *p*-type behavior [26]. Therefore, while C_2N is a promising semiconductor, there is no experimentally validated report demonstrating intrinsic or stable *p*-type properties. Achieving *p*-type C_2N remains an open challenge and a potential area for future research. Controlled acceptor-type doping, combined with careful transport measurements such as Hall effect, FET, or Seebeck characterization, could potentially achieve stable hole conduction and provide a novel contribution to the literature.

The present study highlights the strategic integration of advanced materials and EIS to optimize solar cell performance. By utilizing the unique properties of *p*-C_2N alongside Spiro-OMeTAD and Ni, this work demonstrates the potential for achieving high device performance through efficient light absorption, effective charge transport, and reduced recombination losses at interfaces [27]. EIS offers precise insights into charge dynamics and interfacial interactions that aid in designing better transport layers and minimizing charge recombination, ultimately leading to higher performance and greater commercial viability. Given its wide-ranging applications, IS remains an indispensable tool in the advancement of solar cell technology. Therefore, the findings of this study inspire the potential fabrication and commercial deployment of high-performance graphene-based solar cells in the field of PV technology.

2 | Device Modeling and Simulation

Solar Cell Capacitance Simulator (SCAPS-1D) is a powerful device simulator designed for investigating the electrical and optical properties of thin-film solar cells [28]. Computational simulation is essential for assessing and optimizing solar cell designs, enabling researchers to analyze critical performance parameters without the costs and time associated with experiments [29]. This methodology helps design the most promising configurations and materials for improved solar cell performance, supporting the advancement of more efficient and economically viable solar technologies. The standard illumination power of one sun at 1000 W/m^2 under 1.5 AM [30] was employed. Actual data from published work were used in the modeling and simulation of the proposed cell. The continuity and Poisson's equations for free electrons and holes in the conduction and valence bands are as follows [31]. The continuity equations represent the conservation of charge carriers, including electrons and holes, within a semiconductor. Meanwhile, Poisson's equation connects the electric field in the semiconductor to the density of charge. The continuity equations for electrons and holes and drift-diffusion equations [32, 33] are presented as follows:

$$\nabla^2\Phi = (n - p + N_d - N_a) \tag{1}$$

$$\frac{\partial_n}{\partial_t} = \frac{1}{q}\nabla \cdot J_n + G - U; \frac{\partial_p}{\partial_t} = -\frac{1}{q}\nabla \cdot J_p + G - U \tag{2}$$

$$J_n = qn\mu_n(-\nabla\Phi) + qD_n\nabla_n, J_p = qp\mu_p(-\nabla\Phi) - qD_p\nabla_p \tag{3}$$

where Φ represents the electrostatic potential, n and p denote the electron and hole concentrations, respectively, N_d and N_a are the donor and acceptor doping concentrations, q signifies the electron charge, J_n and J_p refer to the electron and hole current densities, G indicates the carrier generation rate, U stands for the carrier recombination rate, μ_n and μ_p represent the electron and hole mobilities, and D_n and D_p are the electron and hole diffusion coefficients. The Poisson equation is expressed as Equation (4).

$$\frac{d^2}{dx^2}\psi(x) = \frac{e}{\varepsilon_0\varepsilon_r}\left(\rho(x) - n(x) + N_D - N_A + \rho_p - \rho_n\right) \tag{4}$$

here, e represents the electrical charge, ε_r is the relative permittivity, ε_0 is the vacuum permittivity, ψ is the electrostatic potential, p and n denote the concentrations of holes and electrons respectively, N_A and N_D are the concentrations of acceptor and donor charge impurities respectively, and ρ_p and ρ_n are the distributions of holes and electrons respectively [31]. The interaction between the AZO layer and the interface, especially in the presence of the *p*-C_2N (graphitic carbon nitride) active layer, plays a critical role in determining the performance and stability of the model cell structure. The successful integration of AZO in the model cell architecture can result in enhanced operational performance.

2.1 | The Cell Structure and Band Energy Alignment

Figure 1 shows the model cell structure and the band alignment diagram. The core of the cell structure is *p*-C_2N, a two-dimensional semiconductor material that functions as the photoactive layer. Here, light absorption occurs, generating excitons (electron–hole pairs). The final layer, Ni, acts as the back contact. Nickel not only provides a reflective surface that enhances light absorption but also serves as a collector for the holes [34].

The alignment of the energy bands in the proposed solar cell structure is crucial to ensuring effective charge carrier extraction and reducing recombination losses at interfaces. Precisely, the conduction band minimum (CBM) of the absorber should align

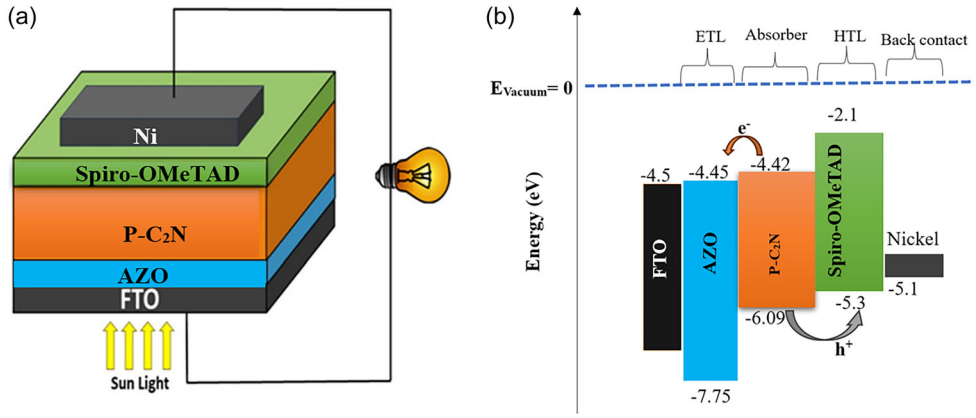

FIGURE 1 | Model cell structure (a) and (b) the corresponding energy band alignment.

with or lie slightly above the CBM of the ETL to enable smooth electron transfer. Likewise, the valence band maximum (VBM) of the absorber should align with or lie slightly below the VBM of the HTL to ensure efficient hole transport. Any misalignment in either case can increase energetic barriers, which prevent carrier extraction and reduce the cell's efficiency. The valence band of p-C_2N displays a nearly ideal band alignment with that of Spiro-OMeTAD, while the conduction band of p-C_2N aligns well with AZO. This favorable alignment ensures efficient separation and transport of excitons, respectively. Therefore, the current cell structure exhibits a good match between the band edges and exhibits a promising carrier transfer at device interfaces. The basic input parameters of the cell are given in Table 1.

3 | Results and Discussion

3.1 | The Absorption Model of the Cell Structure

To model the absorption in the model solar cell architecture, a combination of optical simulations and experimental measurements is typically employed. Optical simulations, such as the transfer matrix method or finite-difference time-domain simulations, are used to model how light propagates through and interacts with each layer [42]. These simulations take into account the refractive index, absorption coefficient, and thickness of each material layer [43]. Experimental measurements, such as UV–vis spectroscopy, are used to measure the absorption spectrum of the p-C_2N layer, while reflectance and transmittance measurements help understand the light reflection by the Ni layer and the light transmission through the FTO and Spiro-OMeTAD layers. The absorption behavior of the device can be determined from the bandgap-dependent square root, Equation (5) [44].

$$\alpha(h\nu) = \left(\alpha_0 + \beta_0 \frac{E_g}{h_V}\right)\left(\sqrt{\frac{h\nu}{E_g}} - 1\right) \tag{5}$$

here, α_0 and β_0 are constants with values, 1.225×10^5 and $10^{-12}\,\mathrm{cm}^{-1}$, respectively.

The absorption coefficient measures how effectively a material absorbs light at specific wavelengths, crucial for assessing a solar cell's light absorption capacity and electricity generation potential. It can be noted that absorption coefficients vary across materials based on photon energy. For instance, p-C_2N exhibits a high absorption coefficient of $\sim 1.5 \times 10^5\,\mathrm{cm}^{-1}$ at 6.2 eV photon energy, implying that the absorption and generation of charge carriers is dominated by the photoactive layers. Accordingly, p-C_2N displays a strong light absorption capability ideal for solar energy harvesting. The absorption coefficient of the HTL

TABLE 1 | The simulation input parameters for the proposed cell structure.

Parameters	Spiro-OMeTAD [35, 36]	p-C_2N [37]	AZO [38, 39]	FTO [40, 41]
Thickness, nm	100	2500	400	100
Bandgap E_g, Ev	3.2	1.67	3.3	3.5
Electron affinity x (eV)	2.1	4.42	4.45	4
Dielectric permittivity	3.0	4.5	9.0	9
CB effective density of states, cm^{-3}	2.5×10^{18}	1×10^{19}	2.2×10^{18}	2.2×10^{18}
VB effective density of states, cm^{-3}	1.8×10^{19}	1×10^{19}	1.8×10^{19}	1.8×10^{19}
Electron mobility, $\mathrm{cm}^2/\mathrm{V\,s}$	2×10^4	1.3×10^1	1×10^2	2.0×10^1
Hole mobility, $\mathrm{cm}^2/\mathrm{V\,s}$	2×10^4	2.06×10^1	2.5×10^1	1.0×10^1
Donor concentration N_D, cm^{-3}	0	0	1.0×10^{18}	2.0×10^{19}
Acceptor concentration N_A, cm^{-3}	1×10^{18}	1×10^{16}	0	0
Defect density, cm^{-3}	1×10^7	1×10^{13}	0	0

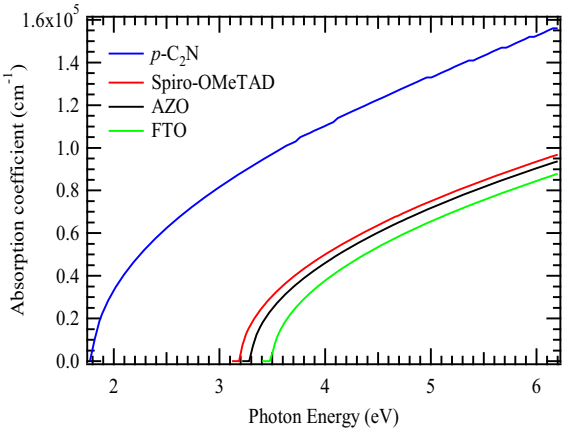

FIGURE 2 | Absorption model of various layers used to make the proposed solar cell architecture.

(Spiro-OMeTAD) has a magnitude of $\sim 9.6 \times 10^4$ at photon energy 6.2 eV, which is significantly lower than that of the photoactive layer. On the other hand, the absorption coefficient for AZO and FTO were lower at $\sim 9.3 \times 10^4$, and $\sim 9.0 \times 10^4$, respectively, at the same photon energy.

Figure 2 shows the absorption coefficient of the materials incorporated in the device configuration, plotted against the wavelength of the incoming electromagnetic radiation. It quantifies the amount of the incident light intensity that gets into a medium as it propagates through it. This attenuation can be modeled using Beer–Lambert's law, expressed by Equation (6).

$$I(x) = I_0 e^{-\alpha x} \tag{6}$$

where $I(x)$ denotes the intensity of the light after penetrating a distance x in the material, I_0 is the initial intensity, and a is the absorption coefficient

3.2 | Effect of Varying the Bandgap of *p*-C_2N On Current Density and Quantum Efficiency (QE)

Figure 3a depicts the effect of varying the bandgap of *p*-C_2N on the solar cell's current density. As the bandgap, increases from 1.4 to 1.9 eV, the V_{oc} improves due to reduced nonradiative recombination and better alignment of the quasi-Fermi levels. However, at a wider bandgap the V_{oc} decreases due to low absorption of lower-energy photons, reducing carrier generation. This emphasizes the importance of optimizing the bandgap to balance V_{oc} and J_{sc} for maximum efficiency. On the other hand, Figure 3b demonstrates the impact of varying the bandgap of *p*-C_2N on the QE. As the bandgap increases, QE declines at longer wavelengths because fewer lower-energy photons are absorbed, consistent with the bandgap energy's cut-off wavelength. Proper bandgap engineering is crucial for maximizing QE within the solar cell's active spectrum.

3.3 | Effect of Varying Defect Density on Current Density and QE

Figure 4 shows that increasing the defect density in the *p*-type C_2N layer markedly reduces both the current density and QE of the solar cell. Higher defect levels create additional recombination centers that trap charge carriers, shorten their lifetimes, and promote nonradiative losses, thereby limiting the number of carriers that can be successfully collected. Figure 4a Impact of different defect densities of the *p*-C_2N layer on the current density of the proposed solar cell architecture. As defect density is increased from 10^{11} to 10^{15} cm^{-3}, there is a clear decline in current density. Lower defect densities, such as 10^{11} and 10^{12} cm^{-3}, result in higher current density values, indicating better cell performance. Conversely, higher defect densities, like 10^{14} and 10^{15} cm^{-3}, significantly reduce current density, highlighting the negative effect of defects on charge carrier collection efficiency. Therefore, reducing defect density in the *p*-C_2N layer is essential for enhancing the solar cell performance. On the other side, Figure 3b demonstrates the relationship between the QE of the proposed solar cell and the defect density of the *p*-C_2N layer. As defect density increases, the QE decreases due to the defects acting as recombination centers for photogenerated carriers, leading to a loss of electron–hole pairs before they reach the electrodes.

The lowest defect density (10^{11} cm^{-3}) has the highest QE, in the range of 85% at 300 nm and 100% between 360 and 700 nm. This observation can be made for defect densities between 10^{11} and 10^{14} cm^{-3}; however, as the defect density reaches 10^{15} cm^{-3}, the QE begins to decrease from 100% between 360 and 400 nm to

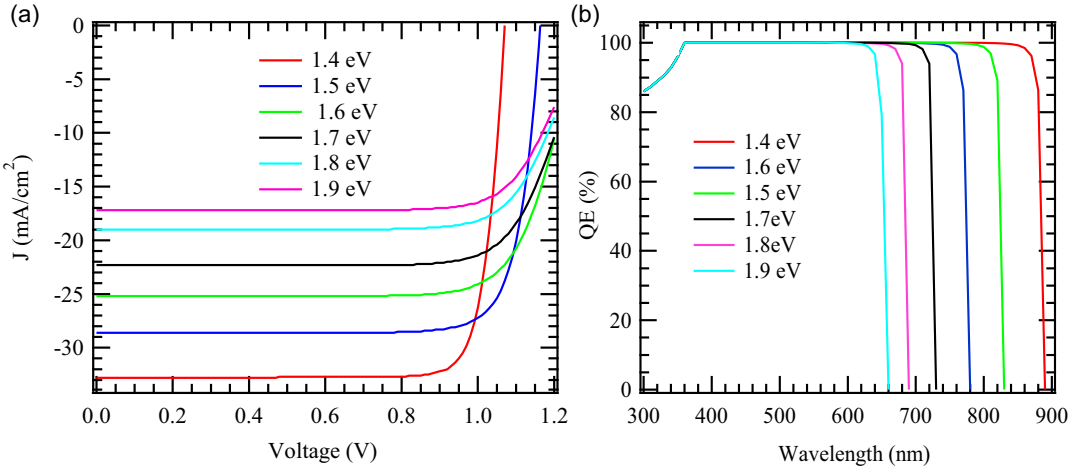

FIGURE 3 | Effect of bandgap on *J*–*V* (a) and (b) QE characteristics.

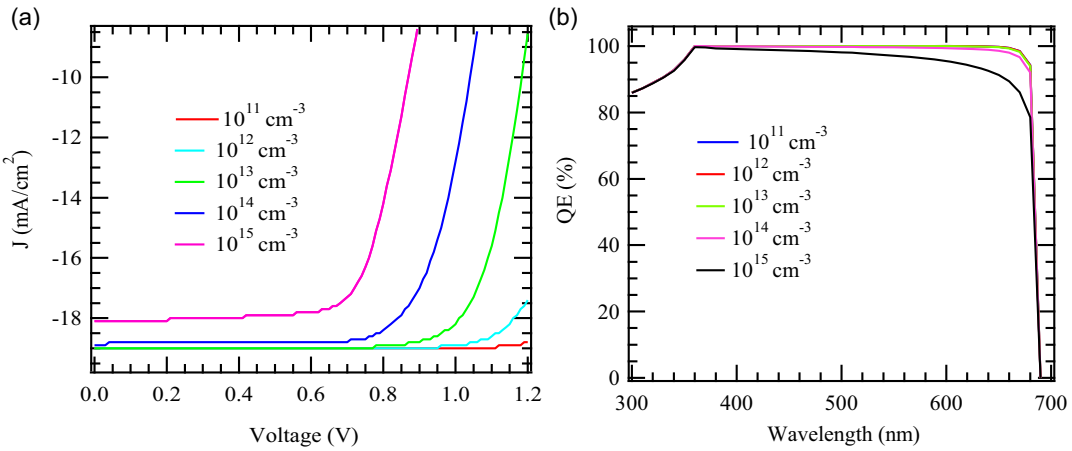

FIGURE 4 | Effect of defect density on *J*–*V* (a) and (b) QE characteristics.

approximately 0% at 700 nm. Thus, minimizing defect density in the *p*-C_2N layer is crucial for maximizing the QE of the solar cell. In essence, the defects act as traps, "capturing" electrons and preventing them from contributing to the measured signal. The defect properties can be described by Equation (7).

$$E_i = E_v + \frac{E_g}{2} + \frac{k_B T}{2}\left(\ln\frac{N_v}{N_c}\right) \tag{7}$$

In this context, E_i is the intrinsic Fermi level, E_v is the energy level of the valence band, and N_c and E_v are the effective density of states for the edges of conduction and valence bands.

4 | Analysis of Conductance, Capacitance, and Complex Impedance

The impedance phase is the angle between the current and the voltage applied at a given frequency. A phase close to 0° indicates purely resistive behavior, while a phase close to −90° indicates purely capacitive behavior. A phase between these values reflects a mixed behavior combining both resistance and capacitance. Therefore, analyzing the phase helps identify transitions between different transport mechanisms, regions of dielectric relaxation, or charge accumulation at the active interfaces of the material. In the very low-frequency range (1 mHz to a few Hz or kHz), the phase is nearly zero or very small, indicating that the current material does not have enough time to move efficiently due to interfacial polarization effects. It reflects the accumulation of trapped charges at the GO/charge transport interface (ETL or HTL), a slow response linked to localized states (defects, thermally induced deformation, or structural distortion), and hopping transport that becomes ineffective at low frequency (Figure 5).

The model cell also exhibits a relaxation at 50 kHz, which corresponds to a charge release phenomenon. A peak or abrupt phase change around 50 kHz indicates a dielectric relaxation, meaning that at this frequency, trapped or polarized charges can be released or reorganized, resulting in maximum energy absorption. The characteristic relaxation time (τ) is approximately 3.18 µs. This corresponds to fast phenomena such as dipole reorientation, electron hopping between localized sites, or charge depolarization at interfaces. A second high-frequency relaxation, which shifts with temperature, is also observed. This frequency shift indicates that the material is temperature-sensitive, which is critical for devices such as solar cells where thermal stability is essential. This behavior reveals the internal dynamics of the material, such as charge mobility and dipolar interactions. Dielectric relaxation represents the delayed response of a material to an alternating electric excitation. At 5 MHz, the excitation period is approximately 0.2 microseconds (µs), meaning that only very fast processes can respond effectively at this frequency. At such high frequencies, charges have very limited time to reorganize.

The analysis of the impedance modulus as a function of frequency and temperature (Figure 6) provides valuable insights into the transport and relaxation mechanisms present in the material. When the temperature is kept constant, it is observed that the impedance modulus remains nearly constant within the frequency range of 1 mHz–1 kHz. This behavior indicates a predominantly resistive response of the material in this very low-frequency range. At this stage, charge carriers are either trapped or only weakly mobile, leading to charge accumulation at interfaces or within localized states, which is typical of a regime dominated by interfacial polarization effects. As the frequency increases beyond this range, the impedance modulus begins to decrease significantly, still under a constant temperature. This decrease suggests that charge carriers become more mobile, and the material enters a relaxation regime where capacitive effects and dynamic conduction mechanisms, such as hopping transport or dipolar reorientation, become significant. This marks the transition from a purely resistive behavior to a mixed behavior (resistance + capacitance).

4.1 | Analyses of the Complex Impedance $Z^*(\omega)$ at different Temperatures

The complex impedance data ($Z^*(\omega) = Z'(\omega) - iZ''(\omega)$) can be analyzed by examining different representations, such as the variation of the real part, $Z'(\omega)$, and the imaginary part, $Z''(\omega)$, with respect to the angular frequency (ω), commonly referred to as Bode plots. Additionally, the evolution of Z'' versus Z', known as Nyquist plots, can also be explored. The coexistence of electronic and ionic conductivities often complicates the elucidation of operational mechanisms in PV devices. Therefore, gaining a

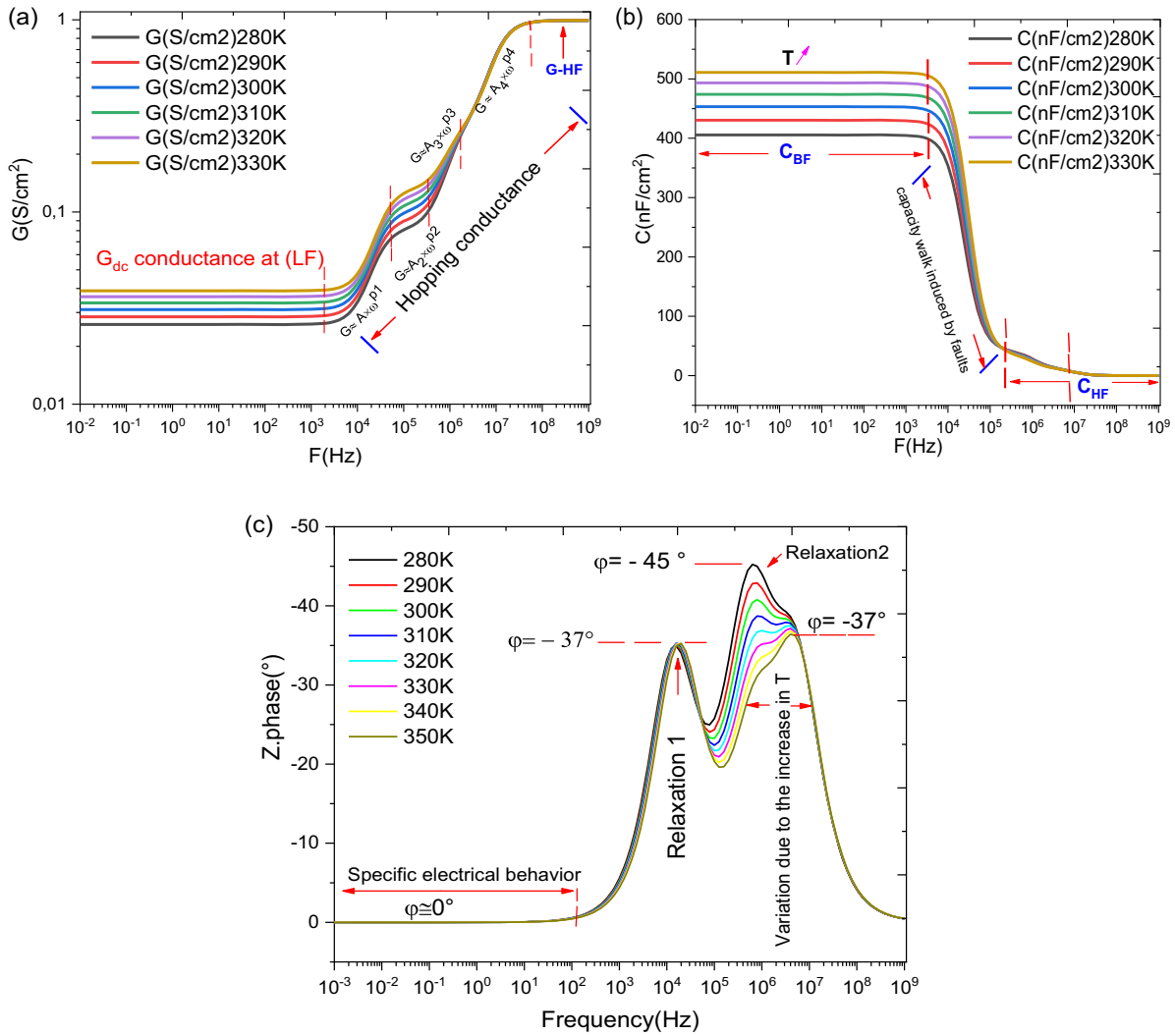

FIGURE 5 | Variation of the conductance (a), capacitance (b), and the phase (c) extracted from the complex impedance of the cell as a function of frequency for all temperatures investigated.

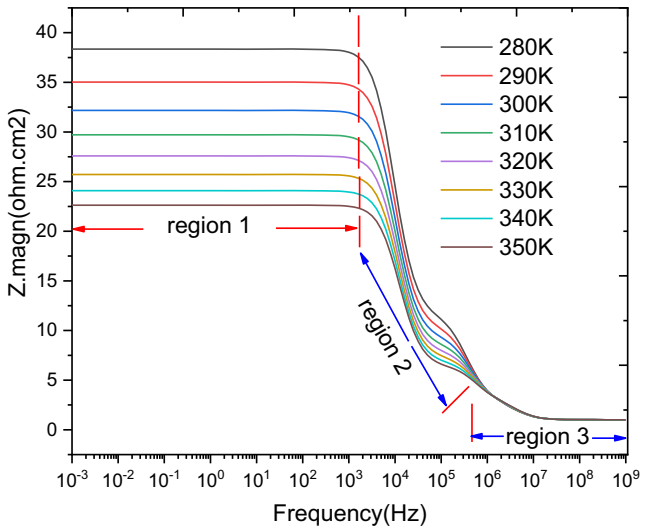

FIGURE 6 | The variation of the complex impedance modulus with frequency across all temperatures.

comprehensive understanding of ionic movement, ion/defect migration, and their impact on solar cell operational mechanisms is crucial for achieving stability and high performance. To tackle this challenge, IS, a widely employed technique capable of investigating these processes across various time scales, is utilized. Therefore, in the following section, the effects of the solar cell performance are investigated through the combination of complex impedance (Z^*) and complex conductivity $\sigma^*(\omega)$.

Figure 7 shows the Nyquist diagram to visualize the different relaxations present in the complex impedance spectrum. This spectrum reveals three relaxations within the frequency range used. The high-frequency relaxation was difficult to distinguish as it is compressed by the subsequent relaxation. For this reason, we performed the deconvolution in Figure 8. The resistance in the Nyquist diagram decreases as the temperature increases, as the resistance decreases due to the rise in temperature.

Figure 7 displays the evolution of the imaginary part as a function of frequency. This representation shows two dielectric relaxations, which illustrate the influence of the permittivity at the

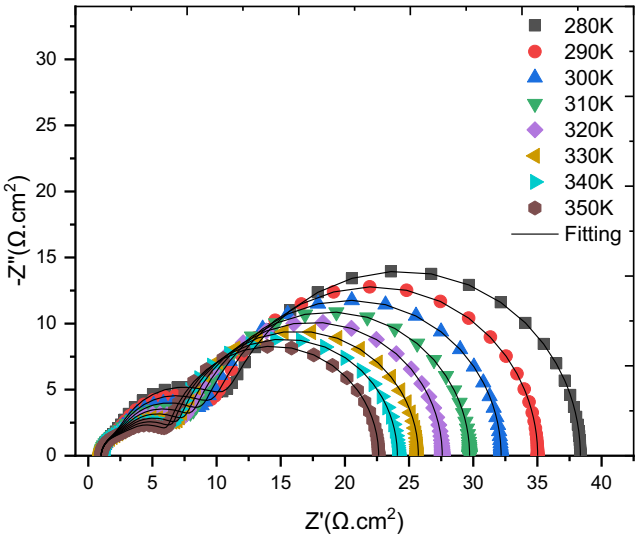

FIGURE 7 | Nyquist diagram for all temperatures.

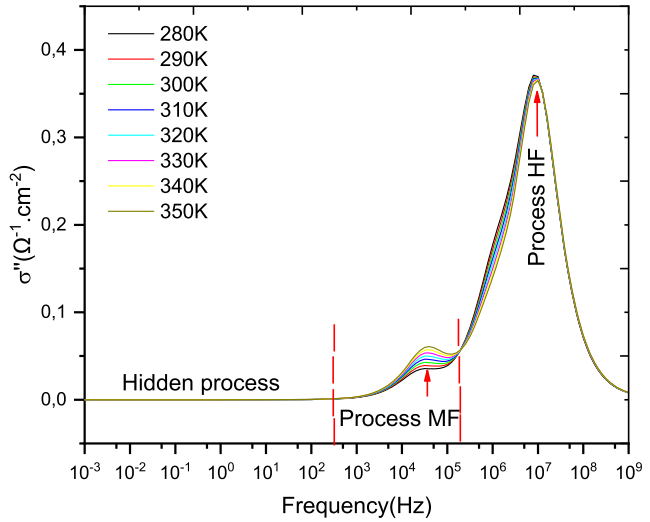

FIGURE 9 | Variation of the imaginary part of conductivity as a function of frequency for all temperatures tested.

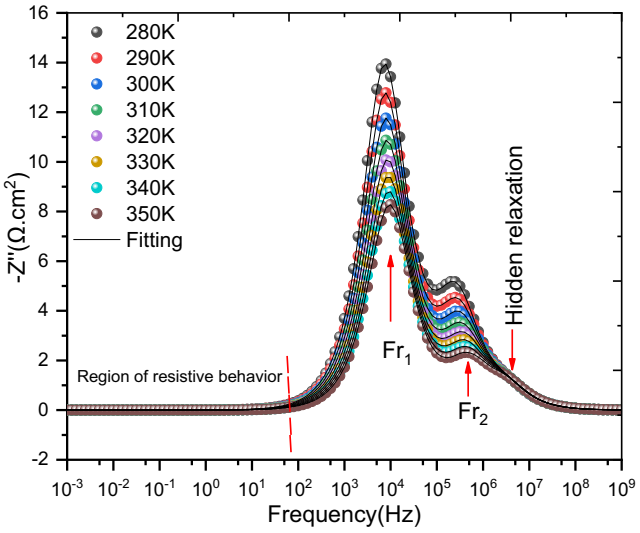

FIGURE 8 | Variation of the imaginary part as a function of frequency for all temperatures investigated.

AZO/FTO and *Spiro-OMeTAD/p-C_2N* interfaces. The plateau observed within this frequency range can be attributed to phenomena related to the formation and organization of the double layer at the AZO/FTO, *p*-C_2N/AZO, and Spiro-OMeTAD/*p*-C_2N interfaces. The interaction with these interfaces may slow down the charge transfer process, especially when the frequency is low enough for charge diffusion effects at the surface to take over [45]. This plateau could also result from polarization effects at the surface of the thin layer, where charges accumulate slowly at the interface [46]. The near-zero value of the imaginary part of the impedance at low frequency indicates that the material exhibits predominantly resistive behavior. This suggests the absence of significant polarization phenomena in this frequency range, likely due to charge accumulation at interfaces or very low carrier mobility. As a result, the system does not display a measurable capacitive response at these low frequencies, reflecting a limitation in charge transport dynamics.

Conductivity measurements indicate that they follow a power-law regime over a wide frequency range, which resembles a q-dc conduction regime. This type of conduction is characteristic of the presence of hopping. However, the various treatments performed on the conductivity measurements through simulation, aimed at highlighting a transport regime via localized states [47], do not allow for a definitive conclusion on the type of hopping regime. The q-dc behavior, however, is due to the dielectric response of the material induced by the movement of charge carriers when they undergo transitions between localized states [48].

Figure 9 displays the evolution of the imaginary part of the complex conductivity as a function of frequency for all temperatures. This representation indicates that this function shows no significant influence when the temperature is increased. Some fluctuations lead to dielectric relaxation at mid-frequency. The imaginary part of conductivity typically reflects the material's response to an alternating electric field, where the charge carriers do not move purely in phase with the applied field, causing a phase shift. At lower frequencies, the imaginary conductivity can indicate the capacitive behavior of the material, where charge carriers accumulate at interfaces or boundaries within the material [49]. However, the absence of strong temperature dependence suggests that the relaxation processes occurring at mid-frequency might be dominated by localized states or interfaces that do not significantly change with temperature, possibly due to saturation of the local dielectric response or thermally activated processes being less influential at these frequencies [50].

Fluctuations in the mid-frequency range could indicate a combination of various relaxation mechanisms, possibly related to interfacial effects or hopping processes that become prominent in this range [49]. These fluctuations can be attributed to the dynamic behavior of charge carriers interacting with localized states or defect states in the material, which govern the dielectric relaxation processes [51]. The relaxation phenomena could also involve the accumulation of charges at interfaces, as discussed in previous studies on complex materials like metal oxides and graphene-based structures [52].

4.2 | Deconvolution Approach for the Conductivity Spectra

Figure 10 shows the Nyquist plot, illustrating the evolution of the imaginary part as a function of the real part of the complex impedance. It also includes the deconvolution of the processes to clarify that there are three blocks, each interpreting the respective contributions that were explained previously in the complex impedance analysis section. Block 1 corresponds to the *AZO/FTO* interface, Block 2 is the *p-C_2N/AZO* interface, which presents a relatively medium recombination resistance, while Block 3 represents the *Spiro-OMeTAD/p-C_2N* interface, which exhibits the highest recombination resistance value. Nyquist plots are essential tools in EIS as they provide insights into the resistive and capacitive contributions of the system.

The analysis of the Nyquist diagram, performed through deconvolution using an equivalent electrical circuit model, reveals the presence of three distinct electrochemical processes occurring within the graphene-based solar cell. These processes are associated with different frequency ranges, a low-frequency process typically related to interfacial charge accumulation or ion migration, a mid-frequency process often linked to trap-assisted transport or polarization effects within the bulk material, and a high-frequency process attributed to rapid electronic responses such as charge displacement or dielectric relaxation at local interfaces.

The Nyquist plot (Figure 10) displays the three processes in the form of semicircles. However, the semicircles are not clearly separated; instead, they appear convoluted, meaning they overlap or merge with each other. This convolution suggests a strong coupling or interaction between the different mechanisms of charge transport and storage in the device. It also reflects the complex and unique electrical behavior of the graphene cell, likely due to the specific nature of graphene's structure and its interfaces with the surrounding materials. Such overlapping responses indicate that the internal dynamics of the device cannot be explained by simple, independent processes, but rather involve interdependent mechanisms acting across a wide range of time constants and frequencies.

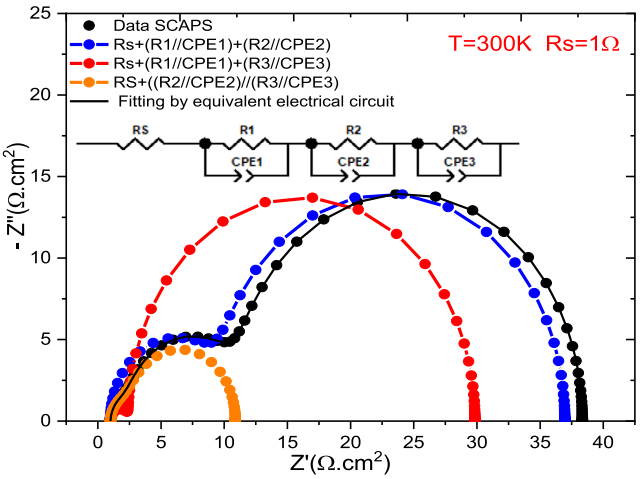

FIGURE 10 | Nyquist diagram for complex conductivity and process deconvolution.

The real part of the impedance reflects resistive elements such as the resistance to charge transfer, while the imaginary part corresponds to the capacitive or inductive behavior of the system, depending on the frequency [53]. In this case, the three blocks show that each interface exhibits different electrochemical behavior. The *AZO/FTO* interface (Block 1) has a relatively low resistance, which suggests efficient charge transfer, whereas the *p-C_2N/AZO* interface (Block 2) depicts medium recombination resistance, suggesting moderate efficiency in charge separation [54]. The *Spiro-OMeTAD/p-C_2N* interface (Block 3), exhibiting the highest recombination resistance, likely demonstrates a slower charge recombination rate, which could enhance the overall efficiency of the PV or electrochemical cell by minimizing energy losses [28, 55]. These variations in recombination resistance are often linked to the quality of the interfaces and the materials used, which affect charge carrier dynamics and the overall device performance. In particular, interfaces with higher recombination resistance tend to suppress charge recombination processes, leading to improved performance [56].

4.3 | Theoretical Consideration for Modeling the Complex Impedance

Building on the previous analysis, we sought to further investigate the complex impedance (Z^*) from a theoretical standpoint, as well as assess the validity of the equivalent circuit presented in Figure 11. This circuit was originally proposed by Ćwil et al. [57] to model the electrical response of perovskite materials. The equivalent circuit consists of a series resistor (Rs) along with three blocks – (R_1//constant phase elements $(CPE)_1$), (R_2//CPE_2), and (R_3//CPE_3), each comprising a resistor in parallel with a constant phase element.

In the above sub-circuit (cf. Figure 11), (CPE-T, p) are used instead of ideal capacitors to account for the distribution of relaxation times caused by surface inhomogeneities [58]. The complex impedance of a (CPE-T, p) is given by Equation (8).

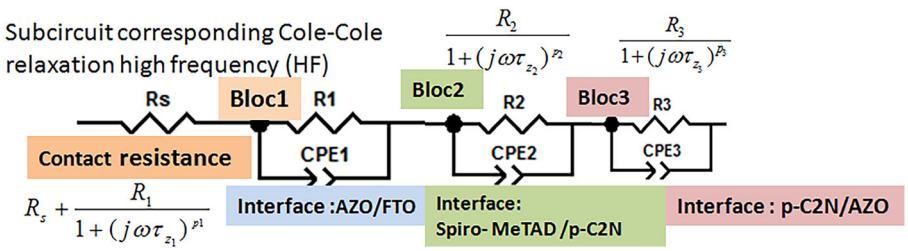

FIGURE 11 | Equivalent circuit used to analyze the complex impedance spectra (Z^*).

$$Z_{\mathrm{CPE}} = \frac{1}{T(j\omega)^{\mathrm{p}}} \tag{8}$$

where T is the pseudocapacitance, ω is the angular frequency, $j^2 = -1$ is the imaginary unit, and p is the exponent characterizing the CPE. The complex impedance $Z^*(\omega)$ of a circuit consisting of R_s in series (R_1//CPE$_1$) can be expressed as shown by Equation (9):

$$Z^*(\omega) = R_s + \frac{R_1}{1 + (j\omega\tau_{Z1})^{p_1}} \tag{9}$$

where (τ_z) denotes the relaxation time:

$$\tau_{z_1} = (R_1 T_1)^{1/P_1} \tag{10}$$

Then decomposition of the complex impedance (Z^*) into its real and imaginary parts results in the following expressions:

$$\tau_{z_1} = (R_1 T_1)^{1/P_1}$$

$$Z'(\omega) = R_s + \frac{R_1\left[1 + (\tau\omega)^{p_1}\cos\left(p_1 \times \frac{\pi}{2}\right)\right]}{\left(1 + (\tau\omega)^{p_1}\cos\left(p_1 \times \frac{\pi}{2}\right)^2 + \left((\tau\omega)^{p_1}\sin\left(p_1 \times \frac{\pi}{2}\right)\right)^2} \tag{11}$$

$$Z''(\omega) = \frac{R_1(\tau\omega)^{p_1}\sin\left(p_1 \times \frac{\pi}{2}\right)}{\left(1 + (\tau\omega)^{p_1}\cos\left(p_1 \times \frac{\pi}{2}\right)^2 + \left((\tau\omega)^{p_1}\sin\left(p_1 \times \frac{\pi}{2}\right)\right)^2} \tag{12}$$

From a theoretical perspective, the critical angular frequency corresponding to the peak can be determined by taking the derivative of the imaginary part of the impedance, $Z''(\omega)$, with respect to the angular frequency ω, and solving the resulting equation: $dZ''(\omega)/d\omega = 0$. In this case, the angular frequency at which the imaginary part of $Z''(\omega)$ reaches its maximum is given by Equations (12 and 13).

$$\omega_{\max 1} = \frac{1}{\tau_{z1}} = \frac{1}{(T_1 R_1)^{1/p_1}} \tag{13}$$

Consequently, the complex impedance $Z^*(\omega)$ can be expressed using a formulation analogous to the one describing the Cole–Cole relaxation process [59, 60].

$$Z^*(\omega) = R_\infty - \frac{Z_s - Z_\infty}{(i\omega\tau_{z1})^p} \tag{14}$$

The overall impedance (Z^*) of the equivalent circuit shown in Figure 11 can be expressed as the sum of the impedances of the sub-circuits corresponding to each individual block as given by Equation (15).

$$Z_g^*(\omega) = R_s + Z_{b1}^*(\omega) + Z_{b2}^*(\omega) + Z_{b3}^*(\omega) \tag{15}$$

In this context, b_1 represents block 1 (AZO/FTO), b_2 represents block 2 (p-C$_2$N/AZO), and b_3 represents block 3 (Spiro-OMeTAD/p-C$_2$N), whereas R_s represents the contact resistance of the electrodes, representing the impedance of the AZO/FTO interface. This represents the impedance of the p-C$_2$N/AZO interface and the Spiro-OMeTAD/p-C$_2$N interface. Such that b_1 = interface (AZO/FTO), b_2 = interface (p-C$_2$N/AZO), and b_3 = interface (Spiro-OMeTAD/p-C$_2$N). To keep consistency with the same notation used in the previous sub-circuit (Figure 11) (R_S *and Block 1*), we can rewrite:

$$Z^*(\omega) = R_s + \frac{R_1}{1 + \left(j\omega\tau_{z_1}\right)^{p_1}} + \frac{R_2}{1 + \left(j\omega\tau_{z_2}\right)^{p_2}} + \frac{R_3}{1 + \left(j\omega\tau_{z_3}\right)^{p_3}} \tag{16}$$

The three expressions corresponding to the relaxation times of each Cole–Cole relaxation process are given in Equations (17a-b).

$$\tau_{z1} = (T_1 R_1)^{\frac{1}{p_1}} \tag{17a}$$

$$\tau_{z2} = (T_2 R_2)^{\frac{1}{p_2}} \tag{17b}$$

$$\tau_{z3} = (T_3 R_3)^{1/p_3} \tag{17c}$$

Therefore, the evolution of the overall complex impedance (Z^*) can be analyzed as the superposition of three Cole–Cole relaxation processes.

4.4 | Activation Energy

The analysis of the conduction mechanism, based on the activation energy (E_a) values, highlights the distinct contribution of each interface. The AZTO/FTO interface exhibits a low activation energy ($E_a = 0.34$ eV), indicating relatively easy charge transport, most likely electronic, through a thermally activated conduction process that is only weakly limited by the interfacial barrier. This region therefore, promotes efficient electron flow toward the FTO and does not represent a major obstacle to conduction. In contrast, the p-CN$_2$/AZO interface, characterized by a moderate activation energy ($E_a = 0.72$ eV), shows more constrained charge transport dominated by a thermally assisted hopping conduction mechanism. This interface introduces an intermediate resistance, probably related to the imperfect alignment of the energy levels between P-CN$_2$ and AZO. Ultimately, the Spiro-OMeTAD/p-CN$_2$ interface, exhibiting the highest activation energy ($E_a = 0.98$ eV), reveals a strongly limited charge transport, most likely of holes, due to a significant interfacial energy barrier. This behavior indicates a conduction process requiring substantial thermal activation and identifies this interface as the main bottleneck of the device, restricting the hole transfer rate toward the top electrode.

Toward this end, the evolution of Equation (18) is plotted on a logarithmic scale, and the graphs displayed in Figure 12a–c are obtained for the three interfaces constituting the cell structure for all temperatures investigated. The evolution shows that the AZO/FTO interface is the most temperature-dependent, followed by the p-C$_2$N/AZO interface, with the Spiro-OMeTAD/p-C$_2$N interface being the least affected. This classification based on activation energy aligns with the changes observed in the electrical resistance of each interface. Activation energy is crucial for understanding the behavior of a solar cell device under temperature variations. This helps to precisely determine the impact of temperature on the electrical parameters and overall cell performance of the cell, as well as assess its thermal stability. From the equivalent circuit using electrical conductivity as a function of temperature and deconvolution, we determine the activation energy for each interface of the

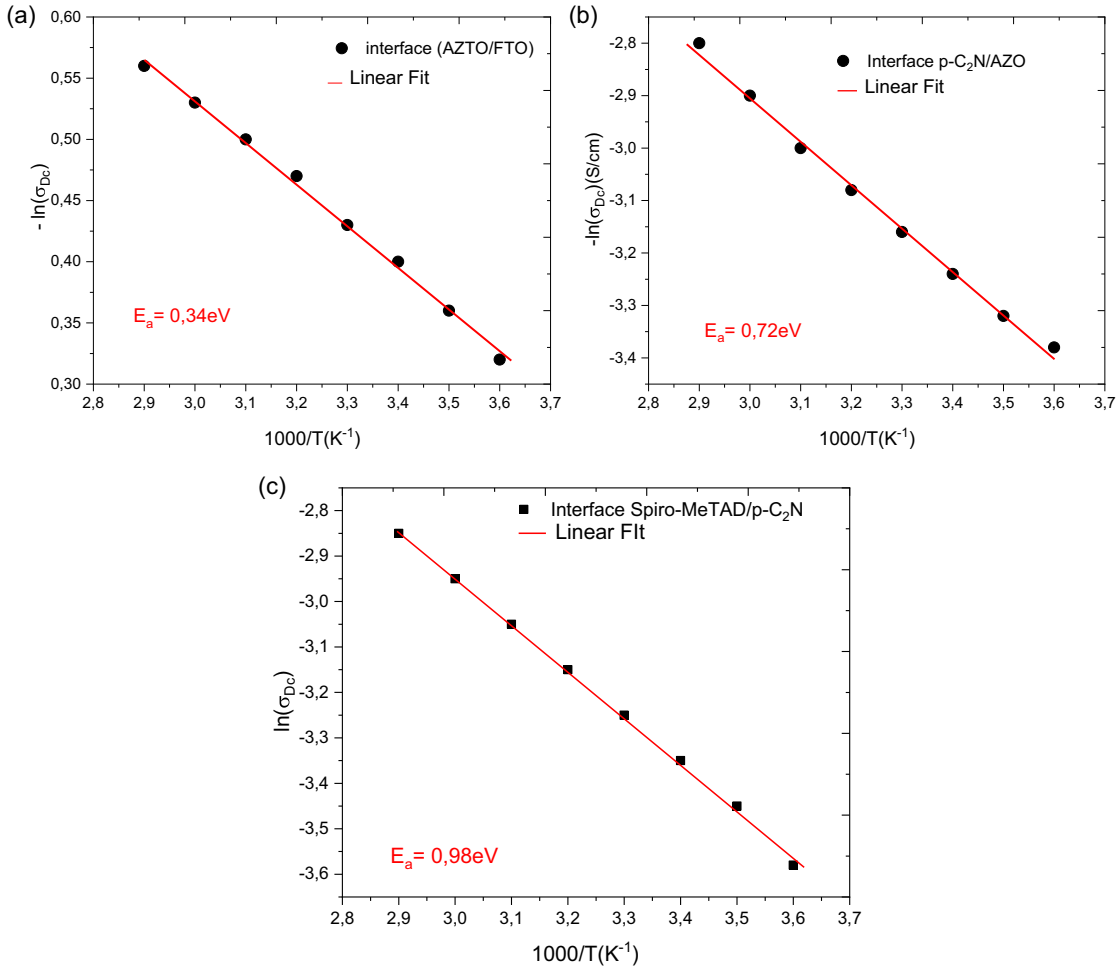

FIGURE 12 | Variation of the activation energy for (a) AZO/FTO, (b) *p*-C_2N/AZO, and (c) Spiro-OMeTAD/*p*-C_2N interfaces.

cell. The expression for the activation energy is defined by Equation (18).

$$\sigma(T) = \sigma_0 \exp\left(\frac{-E_a}{kT}\right) \tag{18}$$

Figure 13a presents the evolution of the relaxation time for each interface. The relaxation time clearly demonstrates that the hopping rate increases with temperature as the relaxation time follows the same trend as the activation energies for the AZO/FTO and *p*-C_2N/AZO interfaces. However, the Spiro-OMeTAD/*p*-C_2N interface indicates the optimal temperature required for better cell performance. According to Figure 13b, charge movement is most efficient at 300 K, where electrons and holes can move and reorganize rapidly between localized sites or at interfaces, minimizing transport losses and

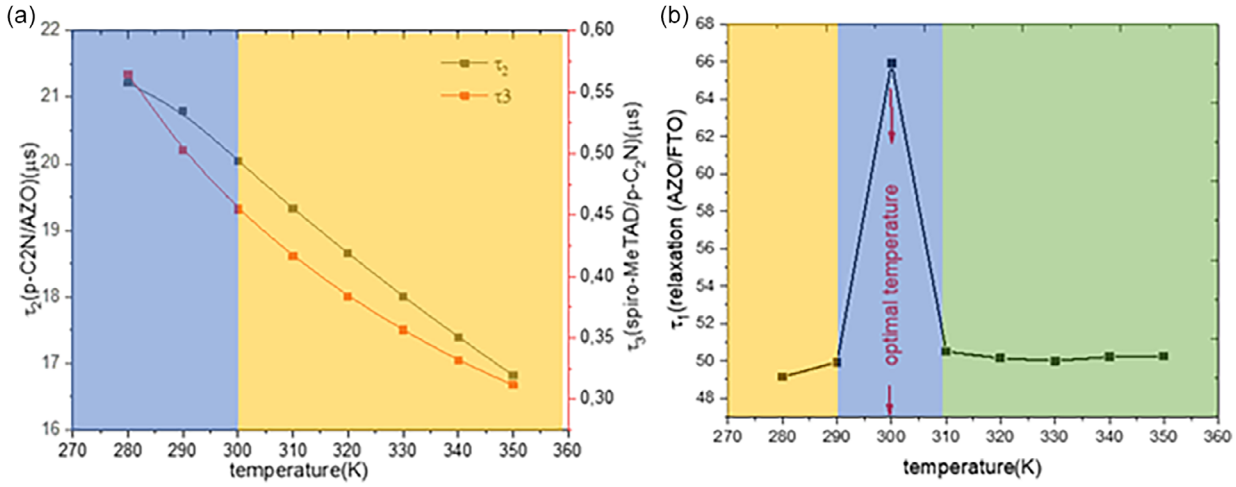

FIGURE 13 | Variation of relaxation times for the (a) *p*-C_2N/AZO and (b) Spiro-OMeTAD/*p*-C_2N interfaces with temperature.

TABLE 2 | Comparative analysis of cell structures based on C_2N-based solar cells.

Configuration	Method	V_{oc}, V	J_{sc}, mA/cm^2	FF, %	PCE, %	Ref.
TCO/IGZO/C_2N/back contact	Simul.	1.50	13.47	84.83	13.11	[61]
Al/TCO/IGZO/C_2N/Pt	Simul.	1.39	17.82	88.95	22.10	[62]
TCO/PCBM/C_2N/back contact	Simul.	1.14	9.58	84.94	9.26	[61]
FTO/AZO/p-C_2N/Spiro-OMeTAD/Ni	Simul.	1.30	23.23	73.84	22.35	This work

maximizing the capacitive/electrochemical response. At lower temperatures (<300 K), charge mobility decreases, leading to a longer relaxation time, while at higher temperatures (>300 K), thermal agitation may cause recombination or disturbances, increasing τ or making it less representative. This optimal relaxation at 300 K suggests that charge conduction and transport are maximized at this temperature, often close to ambient conditions, which is crucial for the performance of devices such as solar cells, batteries, or electrochemical systems.

5 | Comparative Analysis

Table 2 compares the model cell with various solar cell configurations in terms of their performance metrics. Related configurations show lower power conversion efficiency (PCE) values, which may be attributed to mismatches between device layers at interfaces and losses due to charge recombination.

The difference between the current model cell structure (FTO/Spiro-OMeTAD/p-C_2N/Ni) and previous studies reflects the challenges of optimizing photon absorption and charge extraction. Generally, simulations are valuable in establishing theoretical performance limits and guiding material and structural optimizations. However, there is a need to fabricate physical solar cells based on the insights of optimization parameters predicted by theory.

6 | Conclusions

This paper presents an innovative cell architecture – FTO/AZO/p-C_2N/Spiro-OMeTAD/Ni – which has shown considerable potential in operational performance. The optimal electrical outcomes, which include a V_{oc} of 1.303 V, J_{sc} of 23.23 mA/cm^2, fill factor (FF) of 73.84%, and PCE of 22.35% are remarkable. Further, it is evident that at a wavelength of 360 nm, the QE reached 100% with a donor density of between 10^{15} and 10^{20} cm^{-3}. The optimal acceptor density for J_{sc} was observed between 10^{12} and 10^{15} cm^{-3}. Lower bandgaps of the photoactive layer favor the electrical and optical performance of the model cell. For instance, at a bandgap of 1.4 eV of the absorber, the QE is maximum (100%) in the entire wavelength range (300–700 nm), but QE decreases with increasing bandgap of the absorber. From impedance analysis, three conduction mechanisms were identified – low-frequency, hopping, and high-frequency conduction, which contribute to the overall response of the material as a function of frequency and temperature. High-frequency conduction is particularly influenced by the graphene properties at the p-C_2N/AZO interface. The conductivity study highlights that p-C_2N undergoes a sequence of hopping conduction events, which play a crucial role in the operation of the cell. Further, analysis of the impedance spectra and Nyquist plots reveals multiple dielectric relaxations, signifying charge accumulation and discharge phenomena at the material interfaces. From the analysis of the complex impedance (Z^*) in the frequency range [1 mHz–1 GHz], it is found that our theoretical approach, as well as the deconvolution procedure, were very useful in confirming the existence of three distinct Cole relaxation processes involved in the conversion and conduction mechanism in the graphene model solar cell. The three relaxation processes were attributed to the contact resistance in the AZO/FTO, Spiro-MeTAD/p-C_2N, and the p-C_2N/AZO interfaces. Moreover, a detailed analysis of the complex conductivity (σ) through extrapolation and deconvolution procedures over the frequency range [1 mHz–1 GHz] enabled a deeper investigation of the system. Both methods confirmed the presence of three distinct relaxation processes, consistent with observations from the complex impedance (Z) and conductivity (σ^*). According to our theoretical approach, these relaxations resemble the Cole–Cole-type responses associated with the Maxwell–Wagner–Sillars relaxations. This behavior is attributed to local electrostatic interactions between active sites along the graphene molecular chains and counterions at the interfaces, resulting in the formation of induced dipolar moments or diffusion-related mechanisms. This work has revealed remarkable features that help to understand charge dynamics at interfaces and how interface phenomena affect device performance.

Author Contributions

George G. Njema: numerical analysis, methodology, writing – first draft. **Abderrahmane Elmelouky**: method development, numerical analysis, writing & editing. **Chinedu C. Ahia**: resource management & editing. **Edson L. Meyer**: method development & editing. **Joshua K. Kibet**: conceptualization, supervision, and writing & editing. All authors have read and approved the manuscript.

Acknowledgments

The authors wish to sincerely thank Prof Burgelman of the University of Gent, Belgium, for generously allowing us the privilege to access and utilize the SCAPS-1D software. His support has been instrumental in advancing our research endeavors.

Funding

The authors have nothing to report.

Consent

This article has the consent of all the authors.

Conflicts of Interest

The authors declare no conflicts of interest.

Data Availability Statement

The data that support the findings of this study are available from the corresponding author upon reasonable request.

References

1. M. Fazal and S. Rubaiee, "Progress of PV Cell Technology: Feasibility of Building Materials, Cost, Performance, and Stability," *Solar Energy* 258 (2023): 203–219.

2. H. Shan, Y. Yu, R. Zhang, et al., "Electron Transfer and Cascade Relaxation Dynamics of Graphene Quantum Dots/MoS_2 Monolayer Mixed-Dimensional van der Waals Heterostructures," *Materials Today* 24 (2019): 10–16, https://doi.org/10.1016/j.mattod.2019.01.015.

3. N. M. Apandi, W. W. A. Zailani, K. N. K. Izwan, M. Zakaria, and N. N. Zulkarnain, "Graphene Oxide as Carbon-Based Materials: A Review of Geopolymer with Addition of Graphene Oxide towards Sustainable Construction Materials," *Construction and Building Materials* 411 (2024): 134410.

4. Z. Meng, T. Zhang, C. Zhang, Y. Shang, Q. Lei, and Q. Chi, "Advances in Polymer Dielectrics with High Energy Storage Performance by Designing Electric Charge Trap Structures," *Advanced Materials* 36, no. 52 (2024): 2310272.

5. X. Qu and X. Sun, "Impedance Spectroscopy for Quantum Dot Light-Emitting Diodes," *Journal of Semiconductors* 44, no. 9 (2023): 091603.

6. H. Heffner, M. Soldera, F. Ränke, and A. F. Lasagni, "Surface Modification of Fluorine-Doped Tin Oxide Thin Films Using Femtosecond Direct Laser Interference Patterning: A Study of the Optoelectronic Performance," *Advanced Engineering Materials* 25, no. 10 (2023): 2201810.

7. H. Zhang, J. Liu, T. Xu, W. Ji, and X. Zong, "Recent Advances on Small Band Gap Semiconductor Materials (≤2.1 eV) for Solar Water Splitting," *Catalysts* 13, no. 4 (2023): 728.

8. M. F. Rahman, M. K. Hasan, M. Chowdhury, et al., "A Qualitative Design and Optimization of CIGS-Based Solar Cells with Sn_2S_3 Back Surface Field: A Plan for achieving 21.83% Efficiency," *Heliyon* 9, no. 12 (2023): e22866.

9. H. Wu, Y. Cheng, J. Ma, et al., "Pivotal Routes for Maximizing Semitransparent Perovskite Solar Cell Performance: Photon Propagation Management and Carrier Kinetics Regulation," *Advanced Materials* 35, no. 5 (2023): 2206574.

10. S. Kim, W. Lee, Z. Irshad, et al., "Elucidating Interfacial Hole Extraction and Recombination Kinetics in Perovskite Thin Films," *Energies* 17, no. 9 (2024): 2062.

11. M. Rizwan, A. Ayub, S. Urossha, et al., "Organic-Inorganic Perovskite Based Solar Cells," *Perovskite Based Materials for Energy Storage Devices* 151 (2023): 1–32.

12. L. Zang, C. Zhao, X. Hu, J. Tao, S. Chen, and J. Chu, "Emerging Trends in Electron Transport Layer Development for Stable and Efficient Perovskite Solar Cells," *Small* 20, no. 26 (2024): 2400807.

13. G. Regmi, S. Rijal, and S. Velumani, "Aluminum-Doped Zinc Oxide (AZO) Ultra-Thin Films Deposited by Radio Frequency Sputtering for Flexible Cu (In,Ga) Se_2 Solar Cells," *Memories-Materials, Devices, Circuits and Systems* 5 (2023): 100064.

14. G. Yang, W. Yang, H. Gu, et al., "Perovskite-Solar-Cell-Powered Integrated Fuel Conversion and Energy-Storage Devices," *Advanced Materials* 35, no. 44 (2023): 2300383.

15. V. S. Menon, S. Ganesan, R. K. Raman, A. Alagumalai, and A. Krishnamoorthy, "Critical Role of Dopant in NiO_x Hole Transport Layer for Mitigating Redox Reactivity at NiO_x/Absorber Interface in Mixed Cation Perovskite Solar Cells," *Dalton Transactions* 53, no. 2 (2024): 781–797.

16. A. Charnas, Z. Zhang, Z. Lin, et al., "Extremely Thin Amorphous Indium Oxide Transistors," *Advanced Materials* 36, no. 9 (2024): 2304044.

17. P. Kumar, G. Singh, X. Guan, et al., "Multifunctional Carbon Nitride Nanoarchitectures for Catalysis," *Chemical Society Reviews* 52, no. 21 (2023): 7602–7664.

18. M. Singhal, S. Jangir, S. Upadhyay, and D. S. Rajawat, "Advances in Graphitic Carbon Nitride: A Comprehensive Review of Synthesis, Properties, Applications and Recent Developments with Photoelectrochemical Water Splitting," *Discover Chemistry* 1, no. 1 (2024): 64.

19. R. Zhang, B. Li, and J. Yang, "Effects of stacking order, layer number and external electric field on electronic structures of few-layer C_2N-*h*2D," *Nanoscale* 7, no. 33 (2015): 14062–14070.

20. J. Sun, R. Zhang, X. Li, and J. Yang, "A Many-Body GW+ BSE Investigation of Electronic and Optical Properties of C_2N," *Applied Physics Letters* 109, no. 13 (2016): 133108.

21. M. H. Tajarrod, and H. R. Saghai, "High I On/I Off Current Ratio Graphene Field Effect Transistor: The Role of Line Defect," *Beilstein Journal of Nanotechnology* 6, (2015): 2062–2068, https://doi.org/10.3762/bjnano.6.210.

22. Z. Li, P. Zhou, Q. Yan, X. Peng, Z. Ma, and L. Sun, "Second-Order Topological Insulator in Two-Dimensional C_2N and Its Derivatives," *Physical Review B* 106, no. 8 (2022): 085126.

23. P. Jain, R. Rajput, S. Kumar, et al., "Recent Advances in Graphene-Enabled Materials for Photovoltaic Applications: A Comprehensive Review," *ACS Omega* 9, no. 11 (2024): 12403–12425.

24. M.-M. Dong, G.-P. Zhang, Z.-L. Li, M.-L. Wang, C.-K. Wang, and X.-X. Fu, "Anisotropic Interfacial Properties of Monolayer C_2N Field Effect Transistors," *Physical Chemistry Chemical Physics* 22, no. 48 (2020): 28074–28085.

25. M. Yagmurcukardes, S. Horzum, E. Torun, F. M. Peeters, and R. T. Senger, "Nitrogenated, Phosphorated and Arsenicated Monolayer Holey Graphenes," *Physical Chemistry Chemical Physics* 18, no. 4 (2016): 3144–3150.

26. J. Mahmood, E. K. Lee, M. Jung, et al., "Nitrogenated Holey Two-Dimensional Structures," *Nature Communications* 6, no. 1 (2015): 6486.

27. L. Nakka, Y. Cheng, A. G. Aberle, and F. Lin, "Analytical Review of Spiro-OMeTAD Hole Transport Materials: Paths toward Stable and Efficient Perovskite Solar Cells," *Advanced Energy and Sustainability Research* 3, no. 8 (2022): 2200045.

28. G. G. Njema, B. C. Mosonik, C. C. Ahia, and J. K. Kibet, "Modelling and Numerical Evaluation of Photovoltaic Parameters of a Highly Efficient Perovskite Solar Cell Based on Methylammonium Tin Iodide," *Chemistry–A European Journal* 30, no. 71 (2024): e202403192.

29. A. Sharma, A. Sharma, M. Averbukh, et al., "Performance Investigation of State-of-the-Art Metaheuristic Techniques for Parameter Extraction of Solar Cells/Module," *Scientific Reports* 13, no. 1 (2023): 11134.

30. P. Priya, and A. A. Stonier, "Emerging Innovations in Solar Photovoltaic (PV) Technologies: The Perovskite Solar Cells and More," *Energy Reports* 14, (2025): 216–242, https://doi.org/10.1016/j.egyr.2025.06.003.

31. S. K. Biswas, M. K. Mim, and M. M. Ahmed, "Design and Simulation of an Environment-Friendly ZrS_2/$CuInS_2$ Thin Film Solar Cell Using SCAPS 1D Software," *Advances in Materials Science and Engineering* 1 (2023): 8845555.

32. Y. Zhang, Z. Yang, T. Ma, Z. Ai, C. Wang, and X. Li, "A Theoretical Investigation of Transport Layer-Free Homojunction Perovskite Solar Cells via a Detailed Photoelectric Simulation," *Advanced Energy Materials* 13, no. 12 (2023): 2203366.

33. M. Burgelman, P. Nollet, and S. Degrave, "Modelling Polycrystalline Semiconductor Solar Cells," *Thin Solid Films* 361–362 (2000): 527–532, https://doi.org/10.1016/S0040-6090(99)00825-1.

34. A. S. Bati, Y. L. Zhong, P. L. Burn, M. K. Nazeeruddin, P. E. Shaw, and M. Batmunkh, "Next-Generation Applications for Integrated Perovskite Solar Cells," *Communications Materials* 4, no. 1 (2023): 2.

35. N. Rono, A. E. Merad, J. K. Kibet, B. S. Martincigh, and V. O. Nyamori, "Optimization of Hole Transport Layer Materials for a Lead-Free Perovskite Solar Cell Based On Formamidinium Tin Iodide," *Energy Technology* 9, no. 12 (2021): 2100859.

36. S. Hosseini, N. Delibaş, M. Bahramgour, A. T. Mashayekh, and A. Niaei, "Performance Comparison of Different Hole Transport Layer Configurations in a Perovskite-Based Solar Cell Using SCAPS-1D Simulation," *Avrupa Bilim Ve Teknoloji Dergisi*, no. 31 (2021): 121–126, https://doi.org/10.31590/ejosat.951602.

37. T. I. Taseen, M. Julkarnain, and A. Z. M. T. Islam, "Design and Simulation of Nitrogenated Holey Graphene (C_2N) Based Heterostructure Solar Cell by SCAPS-1D," *Heliyon* 10, no. 1 (2024): e23197.

38. Z. Pelawi and H. Alam, "A Numerical Study Of P-Cuo/N-Azo/Thin Film Solar Cells Metal Oxide Based Scaps 1-D," *Jurnal Info Sains: Informatika Dan Sains* 13, no. 02 (2023): 375–378.

39. J. C. Z. Medina, E. R. Andrés, C. M. Ruíz, et al., "Performance Simulation of Solar Cell Based On AZO/CdTe Heterostructure by SCAPS 1D Software," *Heliyon* 9, no. 3 (2023): e14547.

40. M. A. Halim, M. S. Islam, M. M. Hossain, and M. Y. A. Khan, "Numerical Simulation of Highly Efficient Cs2TiI6 Based Pb Free Perovskites Solar Cell with the Help of Optimized ETL and HTL Using SCAPS-1D Software," *Signal and Image Processing Letters* 5, no. 1 (2023): 48–61.

41. S. Abdelaziz, A. Zekry, A. Shaker, and M. Abouelatta, "Investigating the Performance of Formamidinium Tin-Based Perovskite Solar Cell by SCAPS Device Simulation," *Optical Materials* 101 (2020): 109738.

42. C. Park, J. Shin, S. Kim, et al., "Fast and Rigorous Optical Simulation of Periodically Corrugated Light-Emitting Diodes Based On a Diffraction Matrix Method," *Optics Express* 31, no. 12 (2023): 20410–20423.

43. H. P. Pasanen, R. Khan, J. A. Odutola, and N. V. Tkachenko, "Transient Absorption Spectroscopy of Films: Impact of Refractive Index," *The Journal of Physical Chemistry C* 128, no. 15 (2024): 6167–6179.

44. M. Rütten, M. Kaes, A. Albert, M. Wuttig, and M. Salinga, "Relation between Bandgap and Resistance Drift in Amorphous Phase Change Materials," *Scientific Reports* 5, no. 1 (2015): 17362, https://doi.org/10.1038/srep17362.

45. X. Chen, P. V. Kamat, C. Janáky, and G. F. Samu, "Charge Transfer Kinetics in Halide Perovskites: On the Constraints of Time-Resolved Spectroscopy Measurements," *ACS Energy Letters* 9, no. 6 (2024): 3187–3203.

46. L. V. T. Merino, C. E. Petoukhoff, O. Matiash, et al., "Impact of the Valence Band Energy Alignment at the Hole-Collecting Interface On the Photostability of Wide Band-Gap Perovskite Solar Cells," *Joule* 8, no. 9 (2024): 2585–2606.

47. P. R. Barnes, A. Y. Anderson, J. R. Durrant, and B. C. O'Regan, "Simulation and Measurement of Complete Dye Sensitised Solar Cells: Including the Influence of Trapping, Electrolyte, Oxidised Dyes and Light Intensity On Steady State and Transient Device Behaviour," *Physical Chemistry Chemical Physics* 13, no. 13 (2011): 5798–5816.

48. S. Torabi, F. Jahani, I. Van Severen, et al., "Strategy for Enhancing the Dielectric Constant of Organic Semiconductors without Sacrificing Charge Carrier Mobility and Solubility," *Advanced Functional Materials* 25, no. 1 (2015): 150–157.

49. A. Guerrero, J. Bisquert, and G. Garcia-Belmonte, "Impedance Spectroscopy of Metal Halide Perovskite Solar Cells from the Perspective of Equivalent Circuits," *Chemical Reviews* 121, no. 23 (2021): 14430–14484.

50. M. Asandulesa, S. Kostromin, A. Tameev, A. Aleksandrov, and S. Bronnikov, "Molecular Dynamics and Conductivity of a PTB7: PC71BM Photovoltaic Polymer Blend: A Dielectric Spectroscopy Study," *ACS Applied Polymer Materials* 3, no. 10 (2021): 4869–4878.

51. H. F. Haneef, A. M. Zeidell, and O. D. Jurchescu, "Charge Carrier Traps in Organic Semiconductors: A Review On the Underlying Physics and Impact On Electronic Devices," *Journal of Materials Chemistry C* 8, no. 3 (2020): 759–787.

52. B. Sharmila, N. George, S. Sasi, et al., "A Comprehensive Investigation of Dielectric Properties of Epoxy Composites Containing Conducting Fillers: Fluffy Carbon Black and Various Types of Reduced Graphene Oxide," *Polymers for Advanced Technologies* 33, no. 10 (2022): 3151–3162.

53. V. Vivier and M. E. Orazem, "Impedance Analysis of Electrochemical Systems," *Chemical Reviews* 122, no. 12 (2022): 11131–11168.

54. H. Lai and F. He, "Crystal Engineering in Organic Photovoltaic Acceptors: A 3D Network Approach," *Advanced Energy Materials* 10, no. 47 (2020): 2002678.

55. G. O. Odunmbaku, S. Chen, B. Guo, et al., "Recombination Pathways in Perovskite Solar Cells," *Advanced Materials Interfaces* 9, no. 12 (2022): 2102137.

56. G. S. Han, H. S. Chung, B. J. Kim, et al., "Retarding Charge Recombination in Perovskite Solar Cells Using Ultrathin MgO-Coated TiO_2 Nanoparticulate Films," *Journal of Materials Chemistry A* 3, no. 17 (2015): 9160–9164.

57. M. Ćwil, M. Igalson, P. Zabierowski, C. A. Kaufmann, and A. Neisser, "Capacitance Profiling in the CIGS Solar Cells," *Thin Solid Films* 515, no. 15 (2007): 6229–6232.

58. B. Patel, A. Sorrentino, and T. Vidakovic-Koch, "Data-Driven Analysis of Electrochemical Impedance Spectroscopy Using the Loewner Framework," *iScience* 28, no. 3 (2025): 111987, https://doi.org/10.1016/j.isci.2025.111987.

59. K. Górska, A. Horzela, and A. Lattanzi, "Composition Law for the Cole-Cole Relaxation and Ensuing Evolution Equations," *Physics Letters A* 383, no. 15 (2019): 1716–1721, https://doi.org/10.1016/j.physleta.2019.03.008.

60. L. Duan, J. Duan, and M. Li, "Relaxation Functions Interpolating the Cole–Cole and Kohlrausch–Williams–Watts Dielectric Relaxation Models," *Symmetry* 15, no. 6 (2023): 1281, https://doi.org/10.3390/sym15061281.

61. S. Yasin, Z. A. Waar, T. Al Zoubi, and M. Moustafa, "Optoelectronic Simulation of a High Efficiency C_2N Based Solar Cell via Buffer Layer Optimization," *Optical Materials* 119 (2021): 111364.

62. T. I. Taseen, M. Julkarnain, and Islam, "A.Z.M.T.: Design and Simulation of Nitrogenated Holey Graphene (C_2N) Based Heterostructure Solar Cell by SCAPS-1D," *Heliyon* 10, no. 1 (2024): e23197, https://doi.org/10.1016/j.heliyon.2023.e23197